# Spectral turbulence kinetic energy budget and scale-based velocity decomposition for turbulence in bubble plumes $\ensuremath{\mathsepsilon}$

Huijie Wu ; Binbin Wang ■

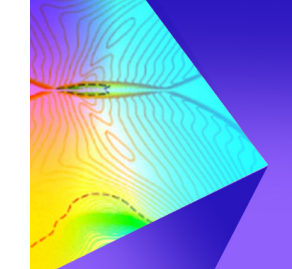


Physics of Fluids 35, 063301 (2023) https://doi.org/10.1063/5.0151046





CrossMark



**Physics of Fluids** 

Special Topic: Shock Waves

**Submit Today!** 



# Spectral turbulence kinetic energy budget and scale-based velocity decomposition for turbulence in bubble plumes

Cite as: Phys. Fluids **35**, 063301 (2023); doi: 10.1063/5.0151046 Submitted: 17 March 2023 · Accepted: 11 May 2023 · Published Online: 1 June 2023









Huijie Wu (i) and Binbin Wang<sup>a)</sup> (i)



#### **AFFILIATIONS**

Department of Civil and Environmental Engineering, University of Missouri, Columbia, Missouri 65211, USA

<sup>a)</sup>Author to whom correspondence should be addressed: wangbinb@missouri.edu

#### **ABSTRACT**

We conducted a spectral analysis of the turbulence kinetic energy (TKE) budget in a bubble plume using particle image velocimetry with fluorescent particles. Our findings confirmed the hypothesis of an inverse energy cascade in the bubble plume, where TKE is transferred from small to large eddies. This is attributed to direct injection of TKE by bubble passages across a wide range of scales, in contrast to canonical shear production of TKE in large scales. Turbulence dissipation was identified as the primary sink of the bubble-produced TKE and occurred at all scales. The decomposition of velocities using the critical length scale of inter-scale energy transfer allowed us to distinguish between large- and small-scale motions in the bubble plume. The large-scale turbulent fluctuations exhibited a skewed distribution and were likely associated with the return flow after bubble passage and the velocities induced by the bubble wake. The small-scale turbulent fluctuations followed a Gaussian distribution relatively well. The large-scale motions contributed to over half of the Reynolds stresses, while there were significant small-scale contributions to the normal stresses near the plume center but not to the shear stress. The large-scale motions in the vorticity field induced a street of vertically elongated vortex pairs, while the small-scale vortices exhibited similar sizes in both horizontal and vertical directions.

Published under an exclusive license by AIP Publishing. https://doi.org/10.1063/5.0151046

### I. INTRODUCTION

Bubbly flows are natural phenomena and widely used engineering applications, including marine hydrocarbon seeps (Wang et al., 2016; Razaz et al., 2020; and Wang et al., 2020), lake aeration for destratifying lakes and reservoirs (Wüest et al., 1992; McGinnis et al., 2006), and prevention of ice formation (Bulson, 1968). Although the mean flow structures and integral behaviors of bubble plumes have been well characterized through experiments, modeling, and theory development (e.g., Mcdougall, 1978; Milgram, 1983; Asaeda and Imberger, 1993; Bryant et al., 2009; Dissanayake et al., 2018; and Wang et al., 2019), the understanding of turbulence in bubble plumes, particularly the mechanisms of turbulence kinetic energy (TKE) transport across eddy scales, remains incomplete.

The challenges in understanding bubble-induced turbulence arise from its multi-scale and nonlinear dynamics that involve the characteristics of two fluid phases. In Richardson's concept of energy cascade, single-phase turbulence is composed of eddies of varying sizes. Although the term "eddy" lacks a precise definition, it generally refers to turbulent motions that occupy a certain area and exhibit moderate correlations (Pope, 2000). According to the Kolmogorov-Richardson phenomenology, in single-phase turbulent flows, TKE is generated at large scales of motion through interactions between shear stress and mean velocity gradient and then successively transferred to smaller scales until it is dissipated by molecular viscosity (Mizuno, 2016; Wang et al., 2021a). In contrast, bubble-induced turbulence is primarily driven by the work of bubble buoyancy rather than shear stress, resulting in an unconventional TKE budget (Lai and Socolofsky, 2019; Wu et al., 2021). In the presence of bubbles of similar sizes, the bubble-induced TKE production is likely associated with a scale relevant to the bubble size. Hence, this bubble-relevant scale in the TKE budget may give rise to a different mechanism of energy cascade. To elucidate this mechanism, we propose a scale-by-scale analysis of the TKE budget as a quantitative description of the energy cascade, which could provide insight into how TKE is generated, transported, and dissipated across different eddy scales.

Two methods have been commonly used for scale-by-scale analysis. Taking homogeneous isotropic turbulence (HIT) as an example, the two dominant processes in the energy cascade are inter-scale energy

transfer and the turbulence dissipation (Pope, 2000). The energy cascade in HIT is precisely characterized by the Karman-Howarth equation, which is derived from the Navier-Stokes equation. Based on Kolmogorov's second hypothesis, the Karman-Howarth equation can be reduced to the Kolmogorov 4/5 law, which neglects the unsteady and viscous terms in the inertial subrange. The Kolmogorov 4/5 law characterizes the energy cascade by equating the third-order structure function, which represents the nonlinear energy transfer, to the turbulence dissipation. However, for flows with insufficient scale separation, where heterogeneity and anisotropy are present, the Karman-Howarth-Monin-Hill (KHMH) equation, a generalized form of the Karman-Howarth equation, must be used to include terms associated with flow heterogeneity and anisotropy, i.e., spatial diffusion, production, and advection (Lai et al., 2018a). The KHMH equation is considered the rigorous approach for analyzing the energy cascade process in heterogeneous and anisotropic turbulence. For example, Alves Portela et al. (2017) applied the KHMH equation to direct numerical simulation (DNS) data and investigated the energy cascade in the near wake of a square prism. They confirmed the forward energy cascade and found that the inter-scale energy transfer is equal to the dissipation rate, validating Richardson's perspective on the energy cascade. Lai et al. (2018a) used the KHMH equation to analyze the energy cascade process in variable density turbulence and confirmed the forward energy cascade. They also observed negative production, in which they attributed to the deformation of small turbulent eddies into larger ones. It is worth noting that the application of the KHMH equation requires a substantially large velocity field to ensure sufficient scale separation in the flow. In experimental studies, this requirement can be met by measuring velocity data at various streamwise locations (Lai et al., 2018a).

Analyzing the TKE budget equation in the spectral domain is an effective method for studying the energy cascade in homogeneous turbulence fields without the requirement of isotropy (Mizuno, 2016; Wang et al., 2021a; 2021b). This method is derived from the spectral form of the Navier-Stokes equation (Bolotnov et al., 2010). For instance, Mizuno (2016) used the spectral TKE budget equation to investigate the contribution of upward and downward energy fluxes in the wavenumber space in a channel flow. They observed that the upward turbulent transport term removes energy from large scales and provides energy to small scales. The energy removed from large scales is transported upward to the channel center and downward to the vicinity of the wall. Wang et al. (2021a) applied the spectral TKE method using DNS data in a turbulent channel flow and found that negative and positive inter-scale TKE transfers are associated with small-scale and large-scale motions, respectively. These energy cascade processes are related to the flow structure with large-scale motions characterized by streaks and quasi-streamwise vortices, while smallscale motions are characterized by hairpin-like vortical structures.

In contrast to applications in single-phase turbulence fields, there are limited attempts for scale-by-scale analyses in multi-phase flows. For instance, Lance and Bataille (1991) performed a simplified version of the spectral TKE budget analysis and argued that bubbles inject energy at small scales, which is immediately dissipated, resulting in a –3 power law in the energy spectrum of bubble-induced turbulence. By studying the time evolution of the energy spectrum in bubbly flows, Mazzitelli and Lohse (2009) found that the energy input on small scales is transferred to large scales, suggesting an inverse energy cascade in bubbly flows. Lai et al. (2018b) used the KHMH equation to

perform a scale-by-scale analysis in a bubble swarm, focusing only on the nonlinear inter-scale energy transfer term, and concluded an inverse energy cascade in bubbly flows. Using the derivative of the third-order structure function, Ma et al. (2022) found an inverse energy cascade in the vertical direction and a forward energy cascade in the horizontal direction. However, a complete spectral budget analysis is still lacking, as the response of other budget terms, such as production, advection, diffusion, and dissipation, to the nonlinear interscale transfer of TKE remains unclear. Therefore, this work is designed to fill this knowledge gap by analyzing all terms in the spectral TKE budget equation in a bubble plume. The main objective of this study is to understand the spectral distribution of all terms in the TKE budget, elucidating the mechanisms governing TKE production, redistribution, and dissipation across various eddies scales in bubble plumes.

In addition, scale-by-scale analysis can be used to identify a critical length scale of turbulent eddies that separates large- and smallscale motions (Wang et al., 2021b). In canonical turbulent flows, including pipe flows and zero-pressure gradient boundary layer flows (Guala et al., 2006; Balakumar and Adrian, 2007), large-scale motions are anisotropic and carry a substantial portion of TKE and shear stress, whereas small-scale motions are statistically isotropic and contribute comparatively less to Reynolds shear stress. However, the applicability of the conventional Kolmogorov hypothesis in the context of twophase phenomenon remains uncertain, given the unconventional TKE injection and dissipation mechanisms directly associated with bubbles (Lance and Bataille, 1991; Wu et al., 2021). To address this issue, we will perform a scale-based velocity decomposition to examine the contribution of motions at various scales to TKE and Reynolds shear stress. This paper is organized as follows: In Sec. II, we describe the measurements and data processing of the bubble plume experiment. The derivation of the spectral energy budget equation is given in Sec. III. Results and discussion of the energy cascade, spectrum of TKE budget terms, velocity statistics, and flow decomposition are presented in Sec. IV. Finally, Sec. V summarizes the conclusions drawn from the study.

# II. EXPERIMENT

#### A. Experimental setup

The laboratory experiment was conducted in the Environmental Fluid Dynamics Laboratory at the University of Missouri. The bubble plume was generated by releasing air bubbles from an airstone diffuser into a quiescent and unstratified water tank. The tank had dimensions of approximately  $1 \times 1 \times 1 \, \text{m}^3$ , with a water depth of 0.87 m. The diffuser was a cylinder-shaped aerator, measuring 2.5 cm in height and 1.5 cm in diameter. The diffuser was positioned at the center of the tank bottom, and the flow rate was precisely controlled at 11/min using a calibrated mass flow controller (SmartTrak 100, Sierra Instruments) (Li *et al.*, 2020; Wu *et al.*, 2021). The experimental setup is shown in Fig. 1.

## B. PIV measurement

The particle image velocimetry (PIV) technique was employed to obtain the instantaneous velocity fields within the bubble plume, which were later used for spectral analysis of the TKE budget. A 10-W diode-pumped solid-state (DPSS) laser (LRS-0532, Laserglow) served as the light source for PIV. The laser beam was expanded into a sheet using a cylindrical lens. PIV images were captured using a high-speed

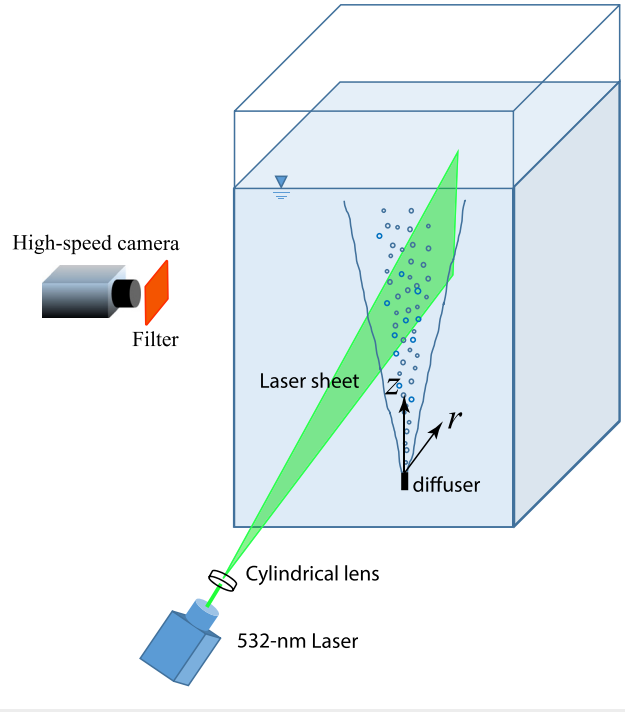


FIG. 1. Sketch of the fluorescent PIV setup.

camera (Phantom VEO 440, Vision Research) at a frame rate of 300 Hz. The field of view (FOV) was  $14.8 \times 9.3 \, \mathrm{cm}^2$  and was centered at a height of 0.46 m above the diffuser. The images had an optical magnification of 0.058 mm/pixel and a full frame size of 2560  $\times$  1600 pixel<sup>2</sup>.

Fluorescent orange polyethylene microspheres were used as seeding particles in the experiment. These particles had a median diameter  $(d_{sp})$  of approximately  $20~\mu m$  and a density  $(\rho_{sp})$  of  $1000~kg/m^3$ , rendering them neutrally buoyant in freshwater at room temperature. The Stokes number (St) was estimated to be on the order of  $10^{-1}$ , calculated as  $St = \rho_{sp}d_{sp}U_f/18\mu$ , where  $U_f = 0.1~m/s$  is the characteristic flow velocity and  $\mu = 10^{-3}$  Pas is the dynamic viscosity of water in the experiment. The small Stokes number satisfied the requirement for the particles to act as tracers for flow following. The fluorescent particles had a peak emission wavelength of 606 nm when excited at 577 nm. To filter out the scattered light by bubbles in the PIV images, a high-pass filter with a cutoff wavelength of 590 nm was used. This ensured that only seeding particles were observed in the PIV images, without any "contamination" from bubbles, allowing for accurate measurement of water velocity (Wu et al., 2021).

The PIV images were directly saved to the camera memory and then transferred to the solid-state drive (SSD) of the operational computer. A continuous dataset of 40 s duration was saved for later analysis. The selection of a 40 s duration was intentional, as it was sufficiently long so that the converged turbulence statistics can be recorded; it was also short enough to minimize the meandering of bubble plume in the dataset. This resulted in a nearly homogeneous turbulence field in the vertical direction, which met the requirement for spectral analysis of the TKE budget.

An anti-aliased PIV interrogation algorithm (Liao and Cowen, 2005) was used to obtain the instantaneous velocity fields in the bubble plume. A prediction-correction method was employed with a final interrogation window size of  $24 \times 24$  pixel², which was equivalent to  $1.4 \times 1.4$  mm². The two-dimensional instantaneous velocities ( $u_{\rm inst}$  and  $w_{\rm inst}$ ) were decomposed into the mean velocity (U and W) and turbulent fluctuation (u and u) using Reynolds decomposition:  $u_{\rm inst} = U + u$  and  $u_{\rm inst} = W + u$ . The Reynolds-averaged turbulent parameters were calculated from the decomposed u and u, e.g., Reynolds normal stresses  $\langle uu \rangle$ ,  $\langle ww \rangle$ , and Reynolds shear stress  $-\langle uw \rangle$ , where the  $\langle \cdot \rangle$  operation denotes time averaging. TKE was calculated using TKE =  $0.5(\langle ww \rangle + 2\langle uu \rangle)$ .

#### C. Measurement uncertainty

The PIV measured instantaneous flow velocity  $u_{\text{inst}}$  is determined from the particle displacement  $\Delta X$  between a consecutive image pair at the time interval  $\Delta t$  (Adrian and Westerweel, 2011),

$$u_{\text{inst}} = \frac{\Delta x}{\Delta t} = \frac{\Delta X}{M\Delta t},\tag{1}$$

where M is the optical magnification, which converts the displacement in the image  $\Delta X$  to that in the physical place  $\Delta x$ . The uncertainty in the PIV measured velocity ( $E_{u_{\text{inst}}}$ ) can be determined using the error propagation formula (Coleman and Steele, 2018),

$$E_{u_{\text{inst}}} = u_{\text{inst}} \sqrt{\left(\frac{E_{\Delta X}}{\Delta X}\right)^2 + \left(\frac{E_M}{M}\right)^2 + \left(\frac{E_{\Delta t}}{\Delta t}\right)^2},$$
 (2)

where  $E_{\Delta X}$ ,  $E_{M}$ , and  $E_{\Delta t}$  represent the measurement error in  $\Delta X$ , M, and  $\Delta t$ , respectively. Among the three error sources,  $E_{\Delta t}$  is negligible when compared to  $\Delta t = 0.0033$  s, because the error in the camera clock is on the order of 1 ns;  $E_{M}$  is also insignificant when appropriate calibration is performed (Sciacchitano, 2019). Therefore,  $E_{u_{\text{inst}}}$  is mainly contributed by the  $E_{\Delta X}$ . Hence, Eq. (2) can be simplified as  $E_{u_{\text{inst}}} = u_{\text{inst}} \frac{E_{\Delta X}}{\Delta X} = \frac{E_{\Delta X}}{M\Delta t}$ .  $E_{\Delta X}$  is estimated as 0.02 pixel according to the PIV algorithm (Liao and Cowen, 2005). Considering M = 17.2 pixel/mm and  $\Delta t = 0.0033$  s,  $E_{u_{\text{inst}}}$  can be determined to be 0.35 mm/s. Given the mean velocity range of 0.015–0.18 m/s across the plume radial direction, the estimated relative errors in velocities fall within the range of 0.2%–2.3%.

### **III. SPECTRAL ENERGY BUDGET EQUATION**

The spectral budget equation is derived by multiplying the Navier–Stokes equation in the Fourier space by the complex conjugate of the corresponding Fourier coefficients of the velocity (Mizuno, 2016; Flores et al., 2017). The Fourier modes of the velocity and pressure fluctuations are denoted as  $\widehat{u}(k,r)$ ,  $\widehat{w}(k,r)$ , and  $\widehat{p}(k,r)$ . Here, u, w, and p are fluctuating components obtained from the Reynolds decomposition of their instantaneous values; k is the wavenumber in the vertical direction, and r is the radial location from the centerline of the bubble plume. The operation  $\widehat{(\cdot)}$  denotes the Fourier transform of each parameter along the vertical direction. Taking the velocity as an example, we have

$$\widehat{u}_i(k,r) = \int_{-\infty}^{\infty} u_i(z,r)e^{-ikz}dz, \tag{3}$$

where the subscript i takes 1 and 3 in the resolved two-dimensional plane (Fig. 1) with  $u_1 = u$  and  $u_3 = w$ .

The spectral TKE budget equation in bubble plumes can be adapted from that of turbulent channel flows (Bolotnov *et al.*, 2010). Note that the advection term is retained in the bubble plume due to radial heterogeneity, and an additional "bubble production" term should be added (Wu *et al.*, 2021), which gives

$$\frac{1}{2} \underbrace{\frac{\partial \langle \widehat{u}_{i} \widehat{u}_{i}^{*} \rangle}{\partial t}}_{\widetilde{A}_{i}} = \underbrace{-U_{k} \frac{\partial \langle \widehat{u}_{i} \widehat{u}_{i}^{*} \rangle}{\partial x_{k}}}_{\widetilde{A}} - Re \left\{ \langle \widehat{u}_{k} \widehat{u}_{i}^{*} \rangle \right\} \frac{\partial U_{i}}{\partial x_{k}}}_{\widetilde{P}} - Re \left\{ \underbrace{\frac{\partial \langle \widehat{u}_{i} \widehat{u}_{k} \widehat{u}_{i}^{*} \rangle}{\partial x_{k}}}_{\widetilde{P}} - Re \left\{ \underbrace{\frac{\partial \langle \widehat{u}_{i} \widehat{u}_{k} \widehat{u}_{i}^{*} \rangle}{\partial x_{k}}}_{\widetilde{T}} \right\}}_{\widetilde{T}_{p}} + \underbrace{\underbrace{\frac{\partial^{2} \langle \widehat{u}_{i} \widehat{u}_{i}^{*} \rangle}{\partial x_{k}^{2}}}_{\widetilde{T}_{\nu}} - \nu \left\langle \underbrace{\frac{\partial \widehat{u}_{i}}{\partial x_{k}} \underbrace{\frac{\partial \widehat{u}_{i}^{*}}{\partial x_{k}}}_{\widetilde{c}}}_{\widetilde{c}} \right\} + \widetilde{P}_{b}.$$
(4)

The physical representation of each term is as follows:

- (1)  $\widetilde{A}_t = \frac{1}{2} \frac{\partial (\widehat{u_t} \widehat{u_t}^*)}{\partial t}$  is the unsteady term in the spectral space, where the superscript \* denotes a complex conjugate. This term is neglected since the turbulence in bubble plumes can be regarded as quasi-steady (Lai and Socolofsky, 2019).
- (2)  $\widetilde{A} = -U_k \frac{\partial \langle \widehat{u}_k u_k^* \rangle}{\partial x_k} \approx -U \frac{\partial \langle \widehat{u}_k \widehat{u}_k^* \rangle}{\partial r}$  is the advection term in the spectral space. The analyzed data in this study span a duration of 40 s and cover a vertical distance of 10 cm, where the turbulence can be treated as nearly homogeneous in the vertical direction (Sec. IV). Thus, the vertical term is neglected, and only the horizontal term is retained.
- zontal term is retained.
  (3)  $\widetilde{P} = -Re\{\langle \widehat{u}_k \widehat{u}_i^* \rangle\} \frac{\partial U_i}{\partial x_k} = -Re\{\langle \widehat{u} \widehat{w}^* \rangle\} \frac{\partial W}{\partial r} Re\{\langle \widehat{u} \widehat{u}^* \rangle\} \frac{\partial U}{\partial r}$  is the shear production term, where  $Re\{\cdot\}$  denotes the real part of a complex variable.
- (4) The nonlinear term  $\widetilde{T} = -Re\{\frac{\partial (\widehat{u_lu_k^{(u_l)}})}{\partial x_k}\}$  includes the inter-scale transfer  $\widetilde{T^{\parallel}}$  and the diffusion in the spectral space  $\widetilde{T^{\perp}}$ , where  $\widetilde{T^{\parallel}} = -Re\{\frac{\partial (\widehat{www^*})}{\partial z}\} 2Re\{\frac{\partial (\widehat{uwu^*})}{\partial z}\}$  with an assumption of  $Re\{\frac{\partial (\widehat{uwu^*})}{\partial z}\} = Re\{\frac{\partial (\widehat{vww^*})}{\partial z}\}$ ;  $\widetilde{T^{\perp}} = -Re\{\frac{\partial (\widehat{wuw^*})}{\partial r}\} 2Re\{\frac{\partial (\widehat{uuu^*})}{\partial r}\}$  with an assumption of  $Re\{\frac{\partial (\widehat{uuu^*})}{\partial r}\} = Re\{\frac{\partial (\widehat{vuv^*})}{\partial r}\}$ . All gradients on the y-direction are neglected.
- (5)  $\widetilde{T}_p = -Re\{\frac{1}{\rho}\frac{\partial \left(\widehat{p}\,\widehat{u}_i^*\right)}{\partial x_i}\}$  represents the pressure–velocity correlation term in the spectral space.

- (6)  $\widetilde{T_{\nu}} = \nu \frac{\partial^2 \langle \widehat{u_i} \widehat{u_i}^* \rangle}{\partial x_{\nu}^2}$  represents the viscous diffusion term in the spectral space.
- (7)  $\widetilde{\varepsilon} = -\nu \langle \frac{\partial \widehat{u}_i}{\partial x_k} \frac{\partial \widehat{u}_i^*}{\partial x_k} \rangle$  represents the turbulence dissipation term in the spectral space.
- (8)  $\widetilde{P}_b$  is the bubble production term in the spectral space.

### IV. RESULTS AND DISCUSSION

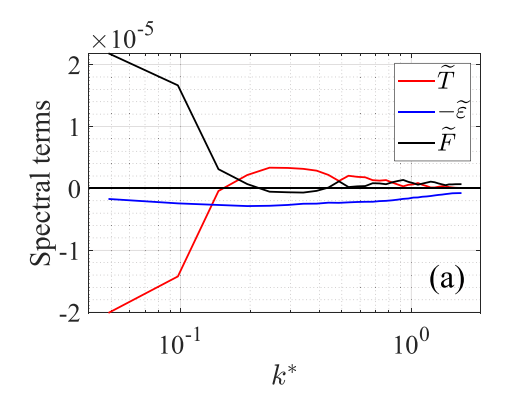
# A. Validation of methodology in homogeneous and isotropic turbulence

The spectral analysis of the TKE budget is first validated using HIT data generated by grid-stirring using a pair of grids (Wu et al., 2023). The data of flow field with the turbulence velocity scale of 0.014 m/s and turbulence dissipation rate of  $3.3 \times 10^{-5}$  m²/s³ are used in this analysis. Due to the absence of mean flow, no advection or shear production is present in the turbulence. Turbulent diffusion of TKE is also negligible due to the homogeneity among all directions. Thus, the original spectral TKE budget equation can be simplified as (Hamba, 2015)

$$\frac{\partial E(k)}{\partial t} = -\widetilde{\varepsilon} + \widetilde{T(k)} + \widetilde{F(k)}. \tag{5}$$

The unsteady term on the left-hand side can be neglected in the quasi-stationary flow. Therefore, in the spectral energy budget of HIT, only three terms appear on the right-hand side: the dissipation term  $\widetilde{\varepsilon}$ , inter-scale energy transfer term  $\widetilde{T}$ , and external forcing term  $\widetilde{F}$ . These three spectral budget terms are plotted in Fig. 2, along with a comparison to those obtained from a numerical simulation (Hamba, 2015).

In Fig. 2(a), the dissipation term and the inter-scale transfer term are directly calculated from the experimental data [Eq. (4)]. The external forcing term  $\widetilde{F}$  is obtained as the closing term. The normalized wavenumber  $k^* = k\eta$  using the Kolmogorov length scale  $\eta$  elucidates the length scale of each term in the budget equation. The profile of the inter-scale transfer term  $\widetilde{T}$  elucidates the mechanism of TKE transport in the spectral space: TKEs of large eddies are primarily transferred to small scales, as evidenced by the negative values of  $\widetilde{T}$  at large wavenumbers and positive values at small wavenumbers. The dissipation term  $\widetilde{\epsilon}$  sinks TKE at all wavenumbers, while the forcing term  $\widetilde{F}$  occurs at large scales, i.e., small wavenumbers. The zero-crossing of  $\widetilde{F}$  is found at  $k^* \approx 0.2$  rad, which corresponds to a length scale of 1.6 cm, similar to the mesh size of the grid. This suggests that the production of turbulence due to grid-stirred forcing occurs at scales larger than the mesh



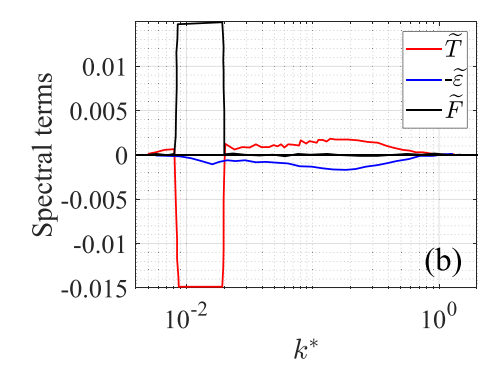


**FIG. 2.** Spectral TKE budget in homogeneous isotropic turbulence: (a) experimental data and (b) numerical simulation data. Panel (b) is reproduced from Hamba (2015). Wavenumber k is normalized by the Kolmogorov length scale  $\eta$ :  $k^* = k\eta$  with a unit of radians. The unit of spectral terms is  $m^3/(s^3 rad)$ .

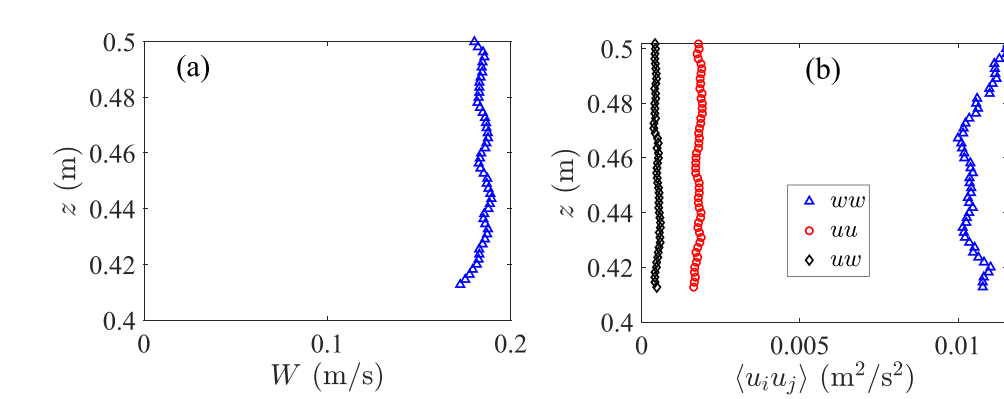


**FIG. 3.** (a) Mean flow velocity and (b) Reynolds stresses along the centerline of the bubble plume.

size of the grid. Subsequently, the inter-scale energy transfer term transfers the TKE from large scales to small scales, and turbulence dissipation takes place across all scales. The mechanism revealed by the spectral analysis of the TKE budget is consistent with the classical Richardson energy cascade (Pope, 2000). Similar results are shown in numerical simulation data [Fig. 2(b)], where the forcing is generated within an idealized range of length scales, resulting in a step-shaped profile in the spectral space (Hamba, 2015).

#### B. Bubble plume

# 1. Homogeneity in the vertical direction

To ensure a valid spectral analysis of the TKE budget, the Fourier transform must be obtained in a direction where turbulence can be assumed to be homogeneous (Hamba, 2015; Mizuno, 2016; and Wang et al., 2021a; 2021b). We examine the assumption of homogeneity in the measured vertical region of the bubble plume along the centerline

(Fig. 3). The data show a reasonable homogeneity of the mean flow W and Reynolds stresses  $\langle ww \rangle$ ,  $\langle uu \rangle$ , and  $\langle uw \rangle$ .  $\langle ww \rangle$  is approximately five times larger than  $\langle uu \rangle$ , indicating a strong anisotropic characteristic of turbulent fluctuations.  $\langle uw \rangle$  is an order-of-magnitude smaller than  $\langle ww \rangle$ , because it is symmetric about the centerline and approaches zero at the plume center.

The third-order statistical quantities play a crucial role in the TKE transport. The data show reasonable homogeneity of the third-order velocity correlations along the centerline of the bubble plume (Fig. 4).  $\langle www \rangle$  is the largest among the resolved four quantities, indicating a strong vertical turbulent flux of the vertical Reynolds stress.

### 2. Spectrum of turbulence dissipation rate

Calculating the turbulence dissipation rate and its spectrum requires estimation of spatial gradients of the instantaneous velocities. Finite differences for the gradients of PIV determined velocities

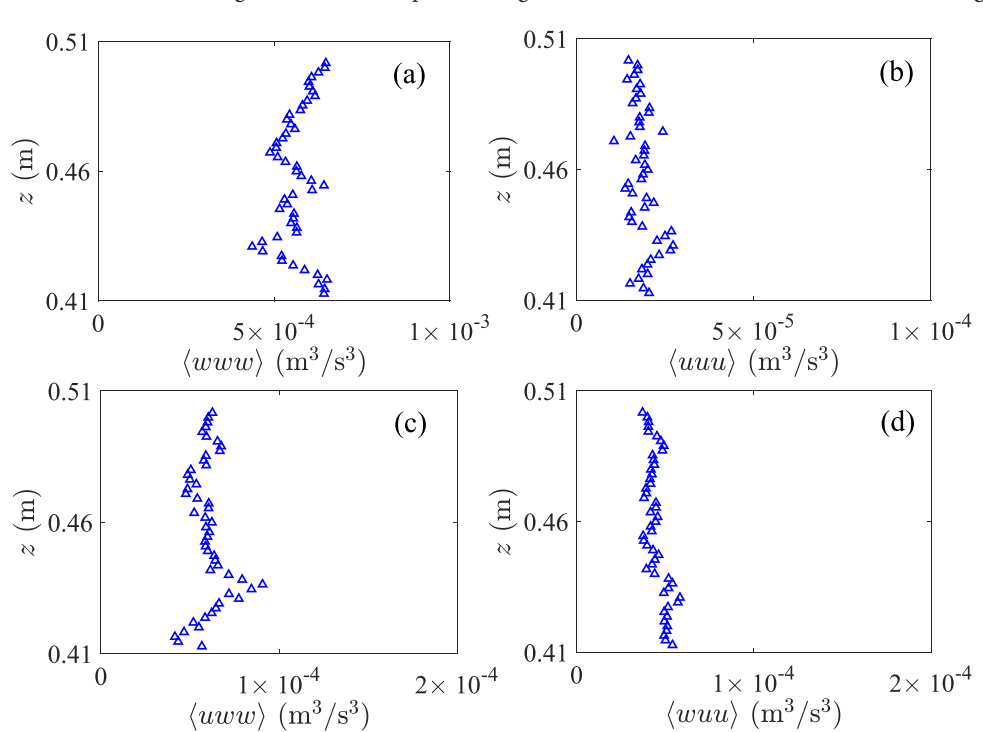


**FIG. 4.** Third order turbulent kinetic energy fluxes along the centerline of the bubble plumes.

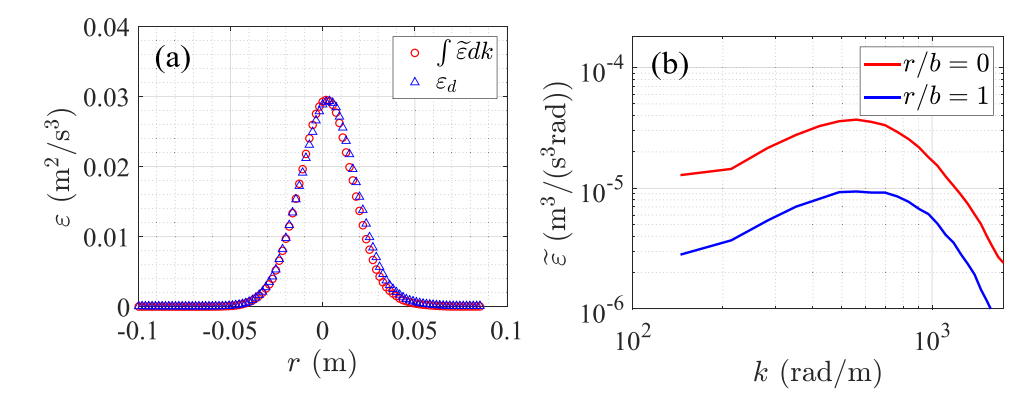


**FIG. 5.** (a) Radial profile of turbulence dissipation rate estimated using  $\varepsilon_d=3\varepsilon_p$  from the resolved PIV data and the integral of turbulence dissipation rate spectrum; (b) profile of turbulence dissipation rate spectrum  $\widetilde{\varepsilon}$  at the plume center (r=0) and at the plume edge (r=b), where b is the plume half-width.

require a grid size that is adequately resolved. In a previous study on bubble plumes (Wu et al., 2021), we used a pseudo expression for turbulence dissipation rate, which was scaled to obtain a reasonable estimate using a one-dimensional velocity spectrum. The pseudo turbulence dissipation rate is given by

$$\varepsilon_{p} = \nu \left[ \left\langle \left( \frac{\partial u}{\partial x} \right)^{2} \right\rangle + \left\langle \left( \frac{\partial u}{\partial y} \right)^{2} \right\rangle + \left\langle \left( \frac{\partial u}{\partial z} \right)^{2} \right\rangle \right. \\
\left. + \left\langle \left( \frac{\partial v}{\partial x} \right)^{2} \right\rangle + \left\langle \left( \frac{\partial v}{\partial y} \right)^{2} \right\rangle + \left\langle \left( \frac{\partial v}{\partial z} \right)^{2} \right\rangle \\
\left. + \left\langle \left( \frac{\partial w}{\partial x} \right)^{2} \right\rangle + \left\langle \left( \frac{\partial w}{\partial y} \right)^{2} \right\rangle + \left\langle \left( \frac{\partial w}{\partial z} \right)^{2} \right\rangle \right]. \tag{6}$$

From the planar PIV data, we determined  $\frac{\partial w}{\partial z}$ ,  $\frac{\partial w}{\partial x}$ ,  $\frac{\partial u}{\partial z}$  and  $\frac{\partial u}{\partial x}$ . Using the continuity equation, we obtained  $\frac{\partial v}{\partial y} = -(\frac{\partial w}{\partial z} + \frac{\partial u}{\partial x})$ . In addition, we estimated  $\frac{\partial u}{\partial y} = \frac{\partial u}{\partial x}$ ,  $\frac{\partial w}{\partial y} = \frac{\partial w}{\partial x}$ ,  $\frac{\partial v}{\partial x} = \frac{\partial v}{\partial y}$ , and  $\frac{\partial v}{\partial z} = \frac{\partial u}{\partial z}$ . A scaling factor  $f_1 = 3$  was determined by comparing  $\varepsilon_p$  estimated in the plume center with that estimated using the spectral fitting method so that  $\varepsilon_s(r=0) = f_1\varepsilon_p(r=0)$ , where  $\varepsilon_s$  was obtained by fitting the universal -5/3-law of the inertial subrange in the one-dimensional velocity spectrum,

$$\varepsilon_s = \left(\frac{E_{33}}{Ck^{-5/3}}\right)^{3/2},\tag{7}$$

where  $E_{33}$  is the spectrum of the vertical velocity in the wavenumber domain resolved in the vertical direction, i.e., k refers to as  $k_3$  or  $k_2$ . The coefficient C takes a value of 0.49 in the main flow direction (Pope, 2000). Because the span of inertial subrange decreases toward the plume edge, Eq. (7) is not used to estimate the turbulence dissipation rate at different radial locations. Instead, a constant factor was determined at the plume center and uniformly applied to all radial locations. After applying the factor  $f_1$  on the pseudo turbulence dissipation rate, we denote the resulting estimate as  $\varepsilon_d = 3\varepsilon_p$ .

The direct calculation of the spectrum of  $\varepsilon$  requires the spectral representation of all nine velocity gradients, similar to the calculation of  $\varepsilon$ . In this study, we computed the one-dimensional spectrum using  $\widetilde{\varepsilon}_{33} = 2\nu k^2 E_{33}$ , which can be later scaled to three dimension (Lai and Socolofsky, 2019). The scaling rule is that the integral of the turbulence dissipation spectrum over the wavenumber domain at each radial

location of the plume should equal the turbulence dissipation rate estimated at that location, i.e.,  $\varepsilon_d(r) = f_2 \int \widetilde{\varepsilon_{33}}(r) dk$  [Fig. 5(a)]. Therefore, the spectrum of  $\varepsilon$  can be estimated as  $\widetilde{\varepsilon} = f_2 \widetilde{\varepsilon_{33}}$ , where  $f_2 = 6$  was determined for our data.

Figure 5(b) shows the spectrum of turbulence dissipation rate at two radial locations. As expected, the turbulence dissipation spectrum near the plume edge (r/b=1) is smaller than that at the plume center (r/b=0), where b represents the half-width of the bubble plume. This observation is consistent with previous findings that indicate higher turbulence dissipation in the center of the plume compared to the edge (Wu et al., 2021). Furthermore, the shapes of the spectra at the two locations show similar wavenumbers of the spectral peak, which aligns with the findings of Pope (2000), who reported consistent peak locations in turbulence dissipation spectra at different Reynolds numbers.

# 3. Spectrum of the inter-scale energy transfer term

The inter-scale energy transfer as shown in Fig. 6 provides insight into the transfer of TKE across different eddy scales in bubble plumes. The data show significant inter-scale energy transfers in the

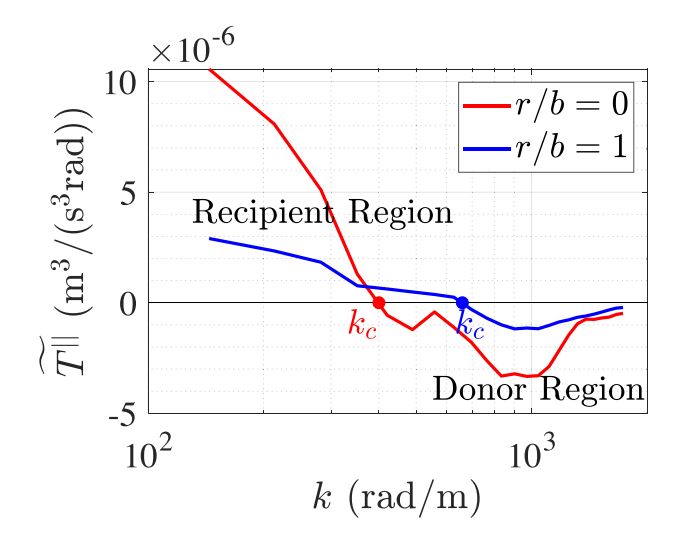


**FIG. 6.** Spectrum of the inter-scale transfer rate in the plume center (r/b = 0) and at the plume edge (r/b = 1).

plume center with weaker transfers observed near the plume edge. Both profiles exhibit a region of the TKE recipient (i.e., positive  $\widetilde{T}^{||}$ ) in large scales (i.e., small wavenumbers) and a region of the TKE donor (i.e., negative  $\widetilde{T}^{||}$ ) in small scales (i.e., large wavenumbers). This behavior can be interpreted as an inverse energy cascade, where the interscale energy transfer moves TKE from small eddies to large eddies, contrary to the classical energy cascade where TKE is transferred from large to small scales (as seen in the HIT profile in Fig. 2). Similar findings of an inverse energy cascade were reported by Lai *et al.* (2018b) in a DNS study of bubble swarm using structure function calculations, and by Mazzitelli and Lohse (2009) who observed a build-up of spectral energy density at high wavenumbers in the instantaneous energy spectrum due to bubble injected energy, followed by a shift toward lower wavenumbers due to the inverse energy cascade.

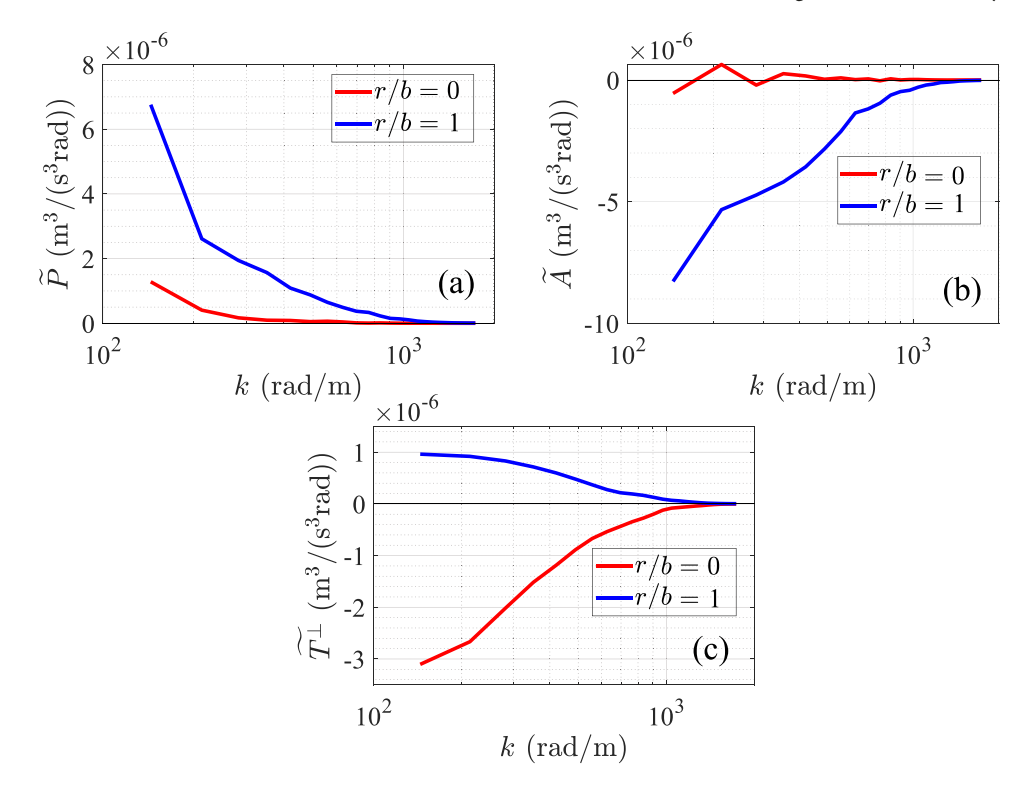
A representative critical wavenumber  $k_c$  can be defined as the zero-crossing point in the spectrum of the inter-scale energy transfer rate, allowing for the examination of a characteristic length scale that distinguishes between large and small motions relevant to TKE sources (Wang et al., 2021b). We will later use  $k_c$  for decomposing the velocity field in the bubble plume (Sec. IV B 6). The data show a smaller  $k_c$  corresponding to a larger critical length scale, in the plume center compared to the plume edge (Fig. 6). This disparity in the critical wavenumber can be associated with the Taylor Reynolds number  $Re_{\lambda} = \frac{u'\lambda}{\nu}$ , where  $\lambda$  is the Taylor micro-scale and u' is the root mean square of turbulent fluctuations (Pope, 2000). As  $Re_{\lambda}$  increases toward the plume center, the range of the energy cascade extends to the low wavenumber region, implying that more large-scale motions are involved in the process of inverse energy cascade as the TKE donor.

# 4. Spectrum of shear production, advection, and diffusion terms

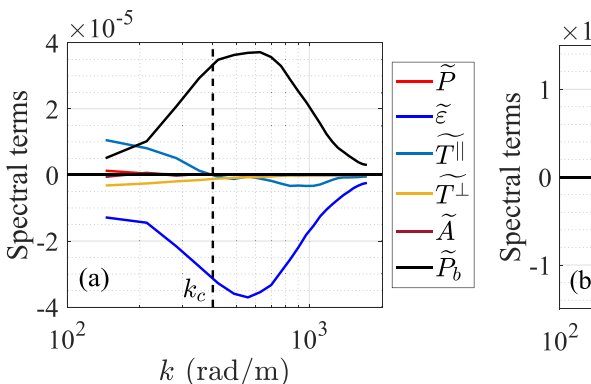
As detailed in Sec. III, the spectral TKE budget equation requires the resolution of additional terms for a complete balance. These terms include a shear production term, a horizontal advection term, and a horizontal diffusion term. The pressure–velocity correlation term, which is a minor contributor to the overall TKE budget (Lai and Socolofsky, 2019), is neglected. The spectra of these terms are computed both in the plume center and near the plume edge, as illustrated in Fig. 7.

The shear production is found to be larger at r/b = 1 compared to r/b = 0, which is attributed to the strong shear present at the plume edge, where the shear stress reaches its maximum value (Wu et al., 2021). The shear production term is positive at all wavenumbers, and its magnitude monotonically decreases with increasing wavenumber, as shown in Fig. 7(a). This indicates that shear production is primarily influenced by the large-scale motions within the bubble plume.

The horizontal advection term  $\widetilde{A}$  is nearly zero at r/b=0 but becomes negative at r/b=1. This behavior is attributed to the product of the horizontal mean velocity and the horizontal gradient of the Reynolds stress, which determines the magnitude of  $\widetilde{A}$ . In the plume center, both the gradient of the Reynolds stress and the horizontal mean flow are close to zero, resulting in a diminished advection term. At r/b=1, we observed that  $\widetilde{A}$  acts as a TKE sink, which is consistent with our previous findings on negative horizontal TKE advection in air-stone bubble plumes for r>0.6b (Wu *et al.*, 2021). Spectral analysis reveals that the advection term is distributed across all wavenumbers with a decreasing contribution from large to small scale motions, leading to a monotonically decreasing trend of  $\widetilde{A}$  with increasing



**FIG. 7.** Shear production spectral term (a), advection spectral term (b), and horizontal diffusion spectral term (c) in the bubble plume.



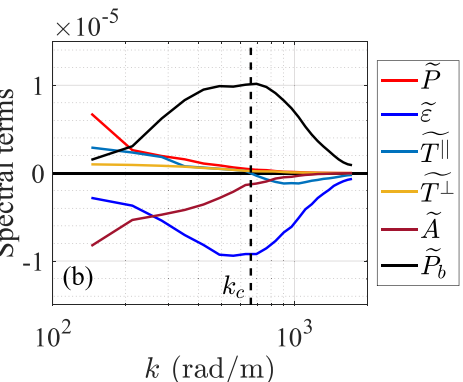


**FIG. 8.** Spectral TKE budget in the bubble plume. (a) Plume center, r/b=0 and (b) plume edge, r/b=1.

wavenumber, as shown in Fig. 7(b). This is in agreement with the recognition of the mean velocity as a characteristic velocity scale for the large eddies in the flow (Pope, 2000).

The spectrum of horizontal diffusion term  $T^{\perp}$  acts as a loss term at the plume center, but as a gain term at r/b=1. This behavior is consistent with the typical diffusion process of redistributing TKE in the radial direction, where higher TKE is moved from the plume center toward the low TKE region far away from the center (Wu *et al.*, 2021). Spectral analysis reveals that the large-scale motions, corresponding to the low wavenumber region, make a stronger contribution to the horizontal diffusion term [Fig. 7(c)]. This is because the majority of turbulent diffusion is determined by the turbulent fluctuations that are comparable to the mean flow (Pope, 2000).

#### 5. Spectral TKE budget

The spectral terms of the TKE budget are shown in Fig. 8 with the TKE injected by bubble passages, referred to as "bubble production," calculated as the closure term in the spectral TKE budget. At the center of the plume, the main contributors to the TKE budget are bubble production  $(\widetilde{P}_b)$ , turbulence dissipation  $(\widetilde{\epsilon})$ , and inter-scale TKE transfer  $(T^{\parallel})$  [Fig. 8(a)]. Bubble production occurs primarily in the small-scale region  $(k > k_c)$ , where  $k_c$  is the critical wavenumber that separates large and small-scale motions in the inter-scale energy transfer. Most of the injected TKE is immediately dissipated at local scales, but a considerable fraction of bubble-generated TKE is transferred to the large-scale motions through the inverse energy cascade with the critical wavenumber corresponding to a length scale of 1.6 cm.

At the edge of the plume, the magnitudes of the spectral TKE budget terms are approximately four times smaller compared to those at the plume center. In addition to  $\widetilde{T}^{\parallel}$ ,  $\widetilde{P}_b$ , and  $\widetilde{\varepsilon}$ , shear production  $(\widetilde{P})$  and horizontal advection  $(\widetilde{A})$  terms are observed to be important at large scales in redistributing TKE. We hypothesize that shear production drives the forward energy cascade, but the overall energy cascade is still dominated by the inverse cascade, as the primary TKE production is through the direct injection from bubble motions. In contrast to the plume center, a significant portion of bubble production occurs at large scales near the plume edge. The large-scale energy generated by bubble production and shear production is not entirely dissipated at local scales. Instead, the excess TKE is balanced by the mean horizontal advection.

#### 6. Scale-based velocity decomposition

The analysis of inter-scale energy transfer provides insight into the inverse energy cascade process in the bubble plume, as discussed in Sec. IV B 3. Additionally, we have identified the critical wavenumber  $k_c$  that serves as a threshold between the recipient and donor regions of TKE in the spectral space during the inverse energy cascade. Therefore, the length scale associated with  $k_c$  can be used as a characteristic eddy scale that distinguishes large and small scales of turbulent motions through velocity decomposition. In this section, we will present velocity statistics, the contribution of large- and small-scale motions to the Reynolds stresses, and the flow structure associated with them.

We use a Fourier-transform-based scale-decomposition technique to separate large- and small-scale motions (Kawata and Alfredsson, 2018; Wang et al., 2021a). First, we take the Fourier transform of the fluctuating velocity u and w to obtain  $\hat{u}$  and  $\hat{w}$ . Next, an inverse Fourier transform is used to obtain the large-scale velocity components, which are enveloped in the wavenumber range of  $-k_c$  to  $k_c$ 

$$w^{L} = \int_{-k_{c}}^{+k_{c}} \widehat{w}(k)dk,$$

$$u^{L} = \int_{-k_{c}}^{+k_{c}} \widehat{u}(k)dk.$$
(8)

The small-scale velocity components can be calculated as  $w^S = w - w^L$  and  $u^S = u - u^L$ .

Prior to discussing the characteristics of the decomposed velocity components, we examine a segment of the time series of fluctuating velocity and its probability density function to gain a better understanding of the flow behavior. An example of the time series of velocity data is presented in Fig. 9 for the plume center and at a radial location of r = 2b. In the plume center [Fig. 9(a)], stronger fluctuations are observed in the vertical velocity component w compared to the horizontal velocity component u. However, at r = 2b [Fig. 9(b)], the magnitude of fluctuations is similar between w and u. The pronounced difference between w and u in the plume center can be attributed to the anisotropic agitating behavior of the bubbles, where the vertical fluctuations are "amplified" by the slip velocity of the bubbles (Wu et al., 2021).

The probability density function (p.d.f.) of velocity fluctuations at r=0 and r=2b is given in Fig. 10, along with the ADV data from a similar bubble plume at  $Q_g=0.5$  l/min as reported in

wu

40

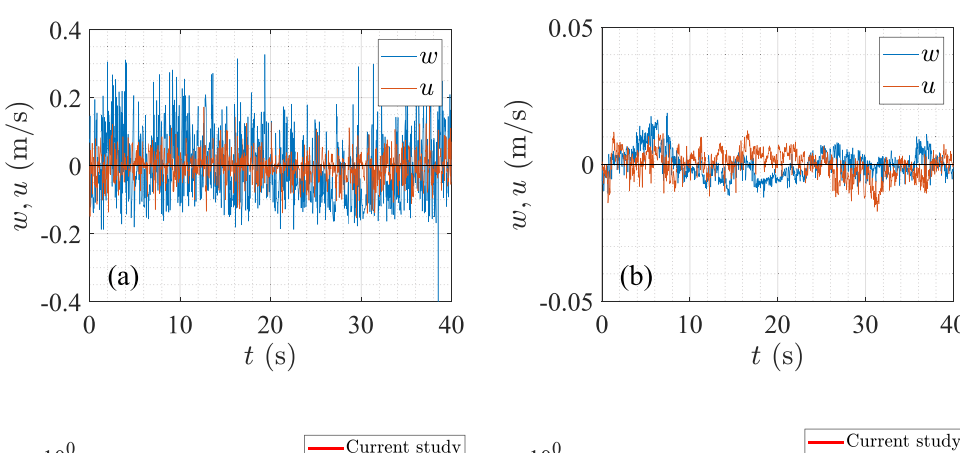
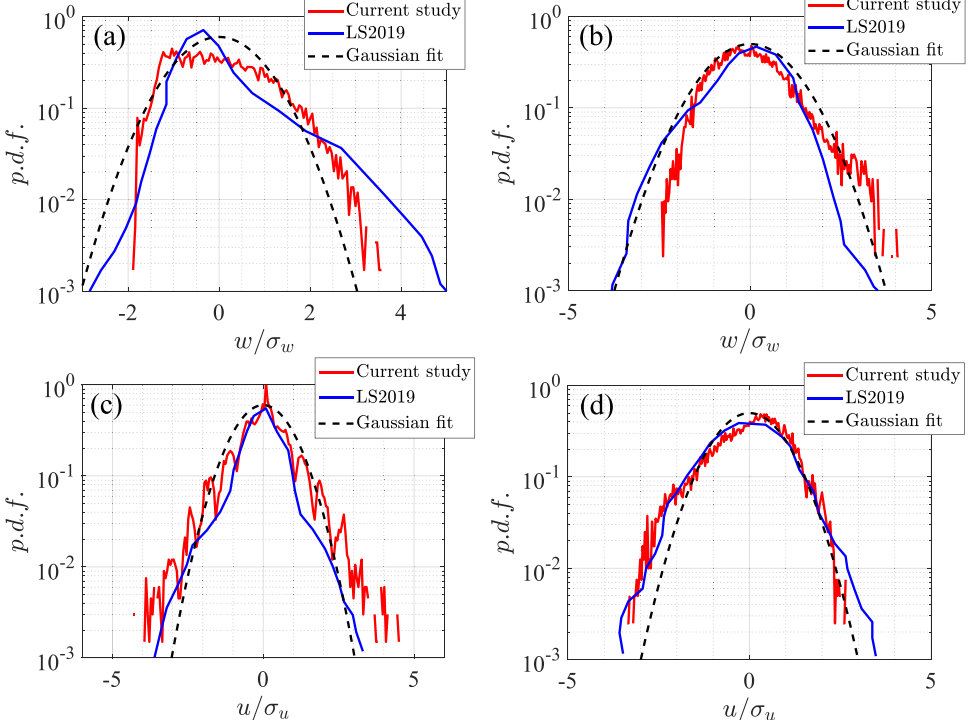


FIG. 9. Time series of the fluctuating velocities u and w. (a) r = 0 and (b) r = 2b.



10. Probability density (p.d.f.) of the fluctuating velocities. (a) Vertical velocities at r = 0; (b) vertical velocities at r=2b; (c) horizontal velocities at r = 0; and (d) horizontal velocities at r = 2b. "LS2019" in the legend represents the ADV data reported in Lai Socolofsky (2019).  $\sigma_u$  and  $\sigma_w$  are the standard deviation of the turbulent fluctuations in the horizontal and vertical directions, respectively.

Lai and Socolofsky (2019) for comparison. In the plume center, the p.d.f. of w exhibits a negative peak and is right-skewed with a positive tail [Fig. 10(a)]. The negative peak is attributed to the return flow of ambient water immediately after the passage of bubbles, while the positive tail is associated with the bubble wake (Lai and Socolofsky, 2019). At r = 2b, the negative peak diminishes, as the likelihood of the bubble passage is reduced [Fig. 10(b)]. The skewness of the distribution is also weaker due to the reduced number of bubbles. On the other hand, the distribution of u closely follows a Gaussian distribution [Figs. 10(c) and 10(d)]. This suggests that the effect of bubble passage primarily influences the distribution of w in the plume.

Using the scale-based velocity decomposition [Eq. (8)], we can analyze the p.d.f. of the large- and small-scale fluctuations, as shown in Fig. 11. The data reveal that the skewed velocity distribution in w is primarily contributed by the large-scale motions, while the small-scale velocities closely follow a Gaussian distribution regardless of the radial location in the plume. As for u, both the large- and small-scale fluctuations exhibit the Gaussian distribution, indicating unskewed horizontal fluctuations at all length scales. This suggests that the effect of bubbles on anisotropic turbulence is prominent in the large scales, where the TKE is inversely cascaded from small-scale motions.

The decomposition of velocity also enables us to examine the contributions of turbulent fluctuations at different scales to the Reynolds stresses. Due to the orthogonal property of the Fourier modes, we have  $\langle w^S w^L \rangle = 0$  and  $\langle u^S u^L \rangle = 0$ . As a result, the Reynolds stresses can be decomposed into large-scale and small-scale components, which are  $\langle ww \rangle = \langle w^L w^L \rangle + \langle w^S w^S \rangle$ ,  $\langle uu \rangle = \langle u^L u^L \rangle + \langle u^S u^S \rangle$ , and  $\langle uw \rangle = \langle u^L w^L \rangle + \langle u^S w^S \rangle.$ 

The radial profiles of decomposed large-scale Reynolds stresses are depicted in Fig. 12. The data demonstrate that the contribution

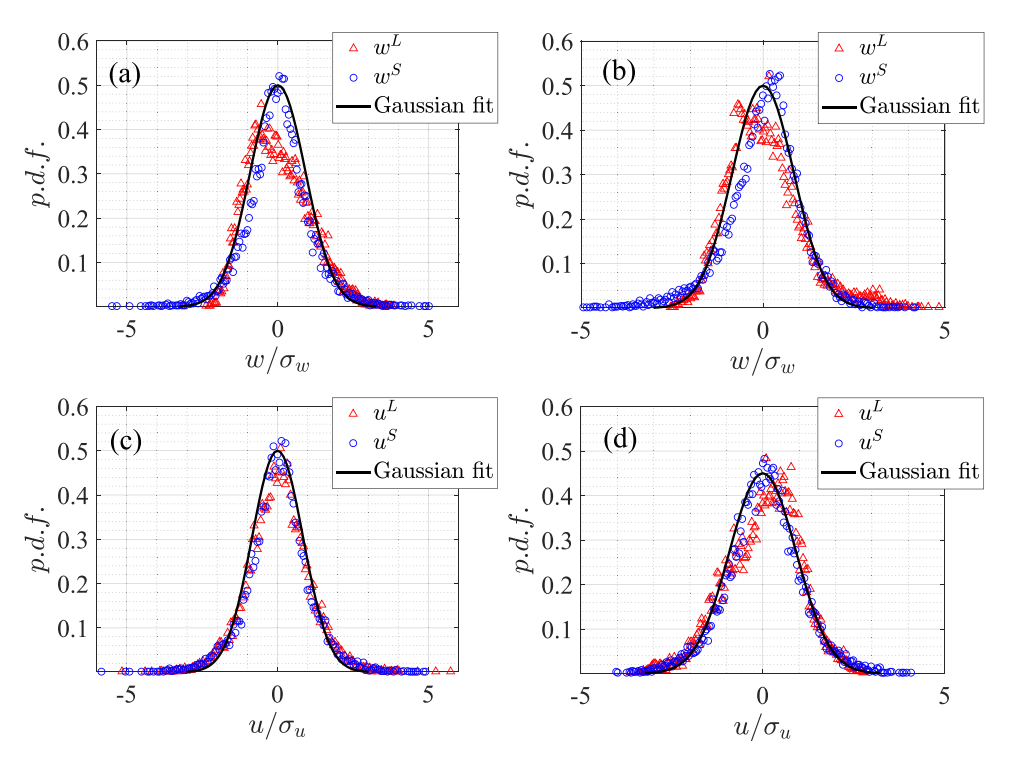
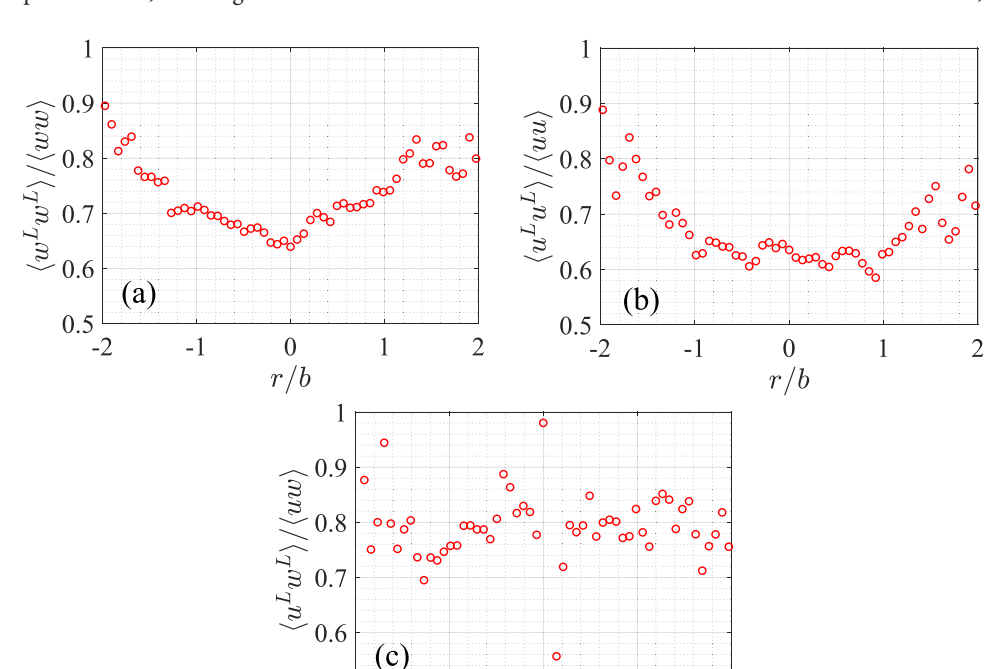


**FIG. 11.** Probability density function (p.d.f.) of the decomposed large- and small-scale velocity fluctuations. (a) Vertical velocities at r=0; (b) vertical velocities at r=2b; (c) horizontal velocities at r=0; and (d) horizontal velocities at r=2b.

to the Reynolds stresses from the large-scale motions is predominant, accounting for more than 50% overall. The contribution of large-scale motions to the normal stresses is suppressed close to the plume center, resulting in a reduction from 80% to 90% at  $r=\pm 2b$ 

0.5

to 60%–70% at r=0 [Figs. 12(a) and 12(b)]. This is due to the substantial contribution of small-scale bubble-induced motions to the normal stresses. On the other hand, the bubble effect is less pronounced in the shear stress, where the large-scale motions contribute



0

r/b

-1

2

**FIG. 12.** Radial profile of the contribution of large-scale motions in Reynolds stresses.

at almost the same level, i.e., approximately 80% within  $|r| \le 2b$  [Fig. 12(c)].

Finally, we examine the vortex structures associated with the large- and small-scale motions. For this purpose, the vorticity is decomposed as follows:

$$\omega = \frac{\partial u_{\text{inst}}}{\partial z} - \frac{\partial w_{\text{inst}}}{\partial x}$$

$$= \left(\frac{\partial U}{\partial z} - \frac{\partial W}{\partial x}\right) + \left(\frac{\partial u^L}{\partial z} - \frac{\partial w^L}{\partial x}\right) + \left(\frac{\partial u^S}{\partial z} - \frac{\partial w^S}{\partial x}\right)$$

$$= \omega^M + \omega^L + \omega^S, \tag{9}$$

where  $u_{\text{inst}}$  and  $w_{\text{inst}}$  are the instantaneous velocities; U and W are the mean velocities; and  $u^L$ ,  $w^L$ ,  $w^S$ , and  $u^S$  are the large- and small-scale fluctuating velocities, respectively. Therefore,  $\omega^M$  represents the vorticity caused by the mean shear, while  $\omega^L$  and  $\omega^S$  represent the vorticity associated with the large- and small-scale motions, respectively. In this study, we refer to them as the large-scale vorticity and small-scale vorticity, respectively.

The decomposed vorticities are illustrated in Fig. 13. For simplicity, we use a constant value of  $k_c=400\,\mathrm{rad/m}$  throughout the flow field, corresponding to 1.6 cm. Note that  $k_c$  increases to 600 rad/m at r=b, equivalent to 1.1 cm. From the vorticity distribution plot, it can be observed that the large-scale vortex structures consist of elongated vortex pairs [Fig. 13(a)], likely caused by the passage of bubbles and eddies of return flows. These elongated vortices have a size of approximately 2 cm in the bubble rise direction and up to 1 cm in the horizontal direction, which are close to the critical value of the inter-scale energy transfer, i.e., 1.1–1.6 cm within the plume region. The small-scale vortex structures [Fig. 13(b)] are smaller in size and similar in both horizontal and vertical directions. Additionally, a pair of weaker but larger mean vortex structures caused by the mean shear can be observed around the plume center. However, these very-large-scale motions contribute little to the TKE compared to the large- and small-scale turbulent motions.

#### V. CONCLUSIONS

A comprehensive spectral analysis of the turbulent kinetic energy (TKE) budget equation is conducted to elucidate the turbulent length scales associated with TKE production, dissipation, and cascade among turbulent eddies in classic bubble plumes. Building upon the critical length scale identified from inter-scale energy transfer, the flow field is further decomposed into large- and small-scale motions to analyze their contributions to the Reynolds stresses and vortex structures.

We first validated the forward energy cascade in homogeneous isotropic turbulence (HIT) by examining the inter-scale energy transfer process. In bubble plumes, we observed an inverse energy cascade, where the TKE is transferred from small-scale to large-scale eddies. The spectral analysis of inter-scale energy transfer is then used to identify a critical wavenumber and its associated length scale. Therefore, a main TKE-recipient region and a TKE-donor region can be separated in the spectral domain.

In the plume center, the TKE budget is dominated by TKE production by bubbles, turbulence dissipation, and inter-scale energy transfer, which occur at both large and small scales. Turbulence dissipation mainly occurs at local scales where TKE is injected from bubble passages, while the remaining TKE is transferred across eddy scales. Away from the plume center, shear production and radial advection of TKE become nontrivial in the TKE budget, and their contribution is mainly at large scales. The inter-scale energy transfer still exhibits an inverse cascade, but with an increased critical wavenumber, indicating a decreased critical turbulent length scale.

The velocity decomposition based on the critical length scale of inter-scale energy transfer allows visualization of the vortex structure associated with large- and small-scale motions. Large-scale swirling motions in the plume are visualized as a street of vertically elongated vortex pairs. Small-scale eddies are observed as scattered vortex pairs with similar sizes in all directions. Additionally, a pair of very-large-scale vortex structures, caused by the mean shear flow in the bubble plume, is present on each side of the plume center.

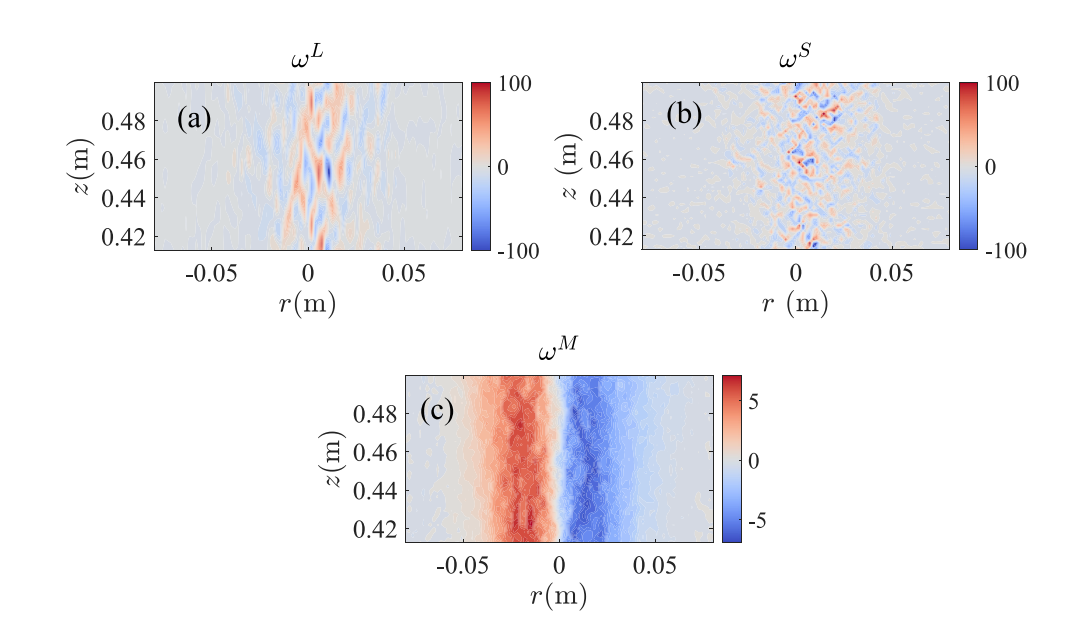


FIG. 13. An snapshot of the decomposed vorticity distribution in the bubble plume: (a) large-scale vortex structure; (b) small-scale vortex structure; and (c) mean vortex structure

Velocity fluctuations at large scales exhibit skewness, while small-scale velocities follow a Gaussian distribution. Reynolds stresses in the bubble plume are mainly contributed by the large-scale motions with bubble effects primarily affecting the normal components. This results in a reduction of the contribution of large-scale Reynolds normal stresses to the total stresses.

#### **ACKNOWLEDGMENTS**

This work was in part supported by the National Science Foundation (Award No. 2049415). The corresponding author is also supported by the Early Career Research Fellowship from the National Academies' Gulf Research Program.

# AUTHOR DECLARATIONS Conflict of Interest

The authors have no conflicts to disclose.

#### **Author Contributions**

Huijie Wu: Conceptualization (supporting); Data curation (equal); Formal analysis (equal); Investigation (equal); Methodology (equal); Validation (equal); Visualization (equal); Writing – original draft (equal); Writing – review & editing (equal). Binbin Wang: Conceptualization (lead); Funding acquisition (equal); Methodology (equal); Supervision (equal); Visualization (equal); Writing – original draft (equal); Writing – review & editing (equal).

#### DATA AVAILABILITY

The data that support the findings of this study are available from the corresponding author upon reasonable request.

# REFERENCES

- Adrian, R. J., and Westerweel, J., Particle Image Velocimetry (Cambridge University Press, 2011).
- Alves Portela, F., Papadakis, G., and Vassilicos, J. C., "The turbulence cascade in the near wake of a square prism," J. Fluid Mech. **825**, 315–352 (2017).
- Asaeda, T., and Imberger, J., "Structure of bubble plumes in linearly stratified environments," J. Fluid Mech. **249**, 35–57 (1993).
- Balakumar, B. J., and Adrian, R. J., "Large- and very-large-scale motions in channel and boundary-layer flows," Philos. Trans. R. Soc., A 365(1852), 665–681 (2007).
- Bolotnov, I. A., Lahey, R. T., Drew, D. A., Jansen, K. E., and Oberai, A. A., "Spectral analysis of turbulence based on the DNS of a channel flow," Comput. Fluids **39**(4), 640–655 (2010).
- Bryant, D. B., Seol, D. G., and Socolofsky, S. A., "Quantification of turbulence properties in bubble plumes using vortex identification methods," Phys. Fluids 21(7), 075101 (2009).
- Bulson, P., "The theory and design of bubble breakwaters," Coastal Eng. Proc. 1(11), 64 (1968).
- Coleman, H. W., and Steele, W. G., Experimentation, Validation, and Uncertainty Analysis for Engineers (John Wiley & Sons, Inc., 2018).
- Dissanayake, A. L., Gros, J., and Socolofsky, S. A., "Integral models for bubble, droplet, and multiphase plume dynamics in stratification and crossflow," Environ. Fluid Mech. 18, 1167–1202. (2018).
- Flores, O., Riley, J. J., and Horner-Devine, A. R., "On the dynamics of turbulence near a free surface," J. Fluid Mech. 821, 248–265 (2017).
- Guala, M., Hommema, S. E., and Adrian, R. J., "Large-scale and very-large-scale motions in turbulent pipe flow," J. Fluid Mech. 554, 521–542 (2006).

- Hamba, F., "Turbulent energy density and its transport equation in scale space," Phys. Fluids 27(8), 085108 (2015).
- Kawata, T., and Alfredsson, P. H., "Inverse interscale transport of the Reynolds shear stress in plane Couette turbulence," Phys. Rev. Lett. 120, 244501 (2018).
- Lai, C. C. K., Charonko, J. J., and Prestridge, K., "A Kármán–Howarth–Monin equation for variable-density turbulence," J. Fluid Mech. 843, 382–418 (2018a).
- Lai, C. C. K., Fraga, B., Chan, R., and Dodd, M. S., "Energy cascade in a homogeneous swarm of bubbles rising in a vertical channel," in *Proceedings of the Summmer Program* (Center for Turbulence Research, 2018b).
- Lai, C. C. K., and Socolofsky, S. A., "The turbulent kinetic energy budget in a bubble plume," J. Fluid Mech. 865, 993–1041 (2019).
- Lance, M., and Bataille, J., "Turbulence in the liquid phase of a uniform bubbly air-water flow," J. Fluid Mech. 222, 95–118 (1991).
- Li, G., Wang, B., Wu, H., and DiMarco, S. F., "Impact of bubble size on the integral characteristics of bubble plumes in quiescent and unstratified water," Int. J. Multiphase Flow 125, 103230 (2020).
- Liao, Q., and Cowen, E., "An efficient anti-aliasing spectral continuous window shifting technique for piv," Exp. Fluids 38, 197–208 (2005).
- Ma, T., Hessenkemper, H., Lucas, D., and Bragg, A. D., "An experimental study on the multiscale properties of turbulence in bubble-laden flows," J. Fluid Mech. 936, A42 (2022).
- Mazzitelli, I. M., and Lohse, D., "Evolution of energy in flow driven by rising bubbles," Phys. Rev. E 79, 066317 (2009).
- Mcdougall, T. J., "Bubble plumes in stratified environments," J. Fluid Mech. 85, 655-672 (1978).
- McGinnis, D. F., Greinert, J., Artemov, Y., Beaubien, S. E., and Wüest, A., "Fate of rising methane bubbles in stratified waters: How much methane reaches the atmosphere?," J. Geophys. Res. 111(C9), C09007, https://doi.org/10.1029/2005JC003183 (2006).
- Milgram, J. H., "Mean flow in round bubble plumes," J. Fluid Mech. 133, 345-376 (1983).
- Mizuno, Y., "Spectra of energy transport in turbulent channel flows for moderate Reynolds numbers," J. Fluid Mech. 805, 171–187 (2016).
- Pope, S. B., Turbulent Flows (Cambridge University Press, 2000).
- Razaz, M., Di Iorio, D., Wang, B., Asl, S. D., and Thurnherr, A. M., "Variability of a natural hydrocarbon seep and its connection to the ocean surface," Sci. Rep. 10, 12654 (2020).
- Sciacchitano, A., "Uncertainty quantification in particle image velocimetry," Meas. Sci. Technol. 30(9), 092001 (2019).
- Wang, B., Jun, I., Socolofsky, S. A., DiMarco, S. F., and Kessler, J. D., "Dynamics of gas bubbles from a submarine hydrocarbon seep within the hydrate stability zone," Geophys. Res. Lett. 47(18), e2020GL089256, https://doi.org/10.1029/2020GL089256 (2020).
- Wang, B., Lai, C. C. K., and Socolofsky, S. A., "Mean velocity, spreading and entrainment characteristics of weak bubble plumes in unstratified and stationary water," J. Fluid Mech. 874, 102–130 (2019).
- Wang, B., Socolofsky, S. A., Breier, J. A., and Seewald, J. S., "Observation of bubbles in natural seep flares at MC 118 and GC 600 using in situ quantitative imaging," J. Geophys. Res. 121, 2203–2230, https://doi.org/10.1002/2015JC011452 (2016).
- Wang, H., Yang, Z., Wu, T., and Wang, S., "Coherent structures associated with interscale energy transfer in turbulent channel flows," Phys. Rev. Fluids 6, 104601 (2021a).
- Wang, W., Pan, C., and Wang, J., "Energy transfer structures associated with large-scale motions in a turbulent boundary layer," J. Fluid Mech. **906**, A14 (2021b).
- Wu, H., Wang, B., Di Iorio, D., and Razaz, M., "Effect of zero-mean shear turbulence on rise velocity of in-chain bubbles from marine natural seeps," Ocean Eng. (to be published).
- Wu, H., Wang, B., DiMarco, S. F., and Tan, L., "Impact of bubble size on turbulent statistics in bubble plumes in unstratified quiescent water," Int. J. Multiphase Flow 141, 103692 (2021).
- Wüest, A., Brooks, N. H., and Imboden, D. M., "Bubble plume modeling for lake restoration," Water Resour. Res. 28(12), 3235–3250, https://doi.org/10.1029/92WR01681 (1992).